Computational Fluid Dynamics Simulation of Fouling on Axial Compressor Stages

Mirko Morini
Michele Pinelli
Pier Ruggero Spina
Mauro Venturini

Engineering Department in Ferrara (ENDIF),
University of Ferrara,
Via Saragat 1,
44122-Ferrara, Italy

Three-dimensional numerical simulations of the effect of fouling on an axial compressor stage were carried out. As a case study, the NASA Stage 37 was considered for the numerical investigation, which was performed by means of a commercial computational fluid dynamic code. The numerical model was validated against the experimental data available from literature. Computed performance maps and main flow field features showed a good agreement with the experimental data. The model was considered representative of a realistic compressor stage. The model was then used to simulate the occurrence of fouling by imposing different combinations of added thickness and surface roughness levels. The effect of fouling on compressor performances was studied. Reductions in the flow coefficient and in the pressure coefficient were found to be of the same order of magnitude of the experimental results found in literature. The model developed seems to overcome some of the limitations of other models found in literature that tend to significantly underestimate the actual values of performance reduction. The numerical results were also used to analyze and debug the stage performance scaling procedure used in stage-stacking models in order to represent fouling in multistage compressors. The analysis highlighted that scaling can adequately represent the behavior of the fouled stage in the choked flow region, but it does not capture the reduction in the maximum of the pressure coefficient, which is instead revealed by the numerical simulations. Finally, blockage due to fouling was investigated both qualitatively and quantitatively.
[DOI: 10.1115/1.4000128]

1 Introduction

The determination of gas turbine operating state consists of the assessment of the modification, due to deterioration and fault, of performance and geometric data that characterize machine components. One of the main effects of deterioration and fault is the modification of compressor and turbine performance maps. Since detailed information about actual modification of component maps is usually unavailable, many authors simulate the effects of deterioration and fault by scaling the map itself. The modification of compressor and turbine performance maps with respect to the *new and clean* condition, due to actual deteriorations and faults, is usually assessed by calculating the map scaling factors through the inverse solution of a program for the calculation of the gas turbine thermodynamic cycle, in order to reproduce the measurements taken on the gas turbine.

Recently, the authors developed a stage-by-stage model to investigate the effects of compressor and turbine stage deterioration [1]. This model uses generalized stage performance curves matched by means of a *stage-stacking* procedure [2].

In this paper, the authors address the most common and experienced source of loss for a gas turbine, i.e., compressor fouling. With respect to the traditional approach, which mainly aims at the identification of the *overall* effects of fouling, in this paper authors investigate a *microscale* representation of compressor fouling (e.g., blade surface deterioration and flow deviation). This allows (i) a more detailed investigation of the fouling effects (e.g., mechanism and location along blade height), (ii) a more extensive analysis of performance deterioration, and (iii) the effect of fouling on stage performance coefficients and on stage performance maps.

In particular, computational fluid dynamics (CFD) simulations of fouling affecting an axial compressor stage were carried out. To do this, the NASA Stage 37 was considered for numerical investigation, which was performed by means of a commercial code. First, the numerical model was set up against experimental data taken from literature in order to obtain a model that was representative of a realistic compressor stage. Then, the model was used to simulate the occurrence of fouling by imposing different combinations of added thickness and surface roughness levels.

2 Literature Survey

In literature, a number of interesting papers on the effects of compressor fouling on gas turbine and compressor performance have been presented. A good review of the main mechanisms and of the effects of fouling on the overall performance of gas turbines can be found in Ref. [3]. In more detail, some papers deal with the analysis of compressor performance deterioration by means of numerical calculations and only a few of them also report experimental data. Finally, in recent decades, the extensive use of CFD three dimensional simulations has also given great insight into flow development in regions experimentally difficult to investigate. Moreover, it has allowed performance variations to be established, which are due to changes in blade geometry or to shape alteration due to corrosion, fouling, erosion, etc.

Bammert and Woelk [4] conducted experimental tests on a three-stage compressor with an increasing blade surface roughness ($k_s/c = 1.5\times10^{-3}$, 2.5×10^{-3}, and 4.5×10^{-3}). They noticed the following: (i) a shift toward lower mass flow rates of the compressor performance maps, (ii) a decrease in the range of mass flow rate at a given rotational speed, and (iii) a decrease in compressor efficiency.

The paper by Suder et al. [5] is a milestone in the development of CFD modeling and in the use of experimental data for the analysis of compressor performance deterioration assessment due to fouling. The paper deals with performance deterioration of a high-speed axial compressor rotor, the NASA Rotor 37, due to artificially imposed alterations in terms of surface roughness in the range 0.508–3.18 μm and airfoil thickness variations. Then,

Contributed by the International Gas Turbine Institute (IGTI) of ASME for publication in the JOURNAL OF ENGINEERING FOR GAS TURBINES AND POWER. Manuscript received April 9, 2009; final manuscript received April 10, 2009; published online April 8, 2010. Editor: Dilip R. Ballal.

a quasi-3D Navier–Stokes flow solver is used to simulate these alterations and the comparison with the experimental data is reported. Among the numerous and very interesting results, the most significant for this present paper are as follows: (i) Degradation does not significantly affect the stall line; (ii) the maximum mass flow achieved by the altered rotor is lower than that of the baseline rotor at all rotational speeds; (iii) at constant pressure rise, the efficiency losses are in the region of 2.5–6.5% for the thickened smooth surface and 6.0–8.5% for the thickened rough surface; (iv) a 9% loss in pressure ratio across the rotor when near the design flow is observed for rough surfaces. Finally, they found that compressor performance characteristics predicted by CFD calculations are sensitive to the addition of surface roughness to the numerical model, but at the same time they found that the roughness model significantly underpredicts the performance changes with respect to the measured ones.

More recently, Gbadebo et al. [6] presented the results of experiments and numerical simulations performed on a large-scale single-stage low-speed compressor. The experimentally imposed roughness was chosen by scaling roughness measurement values obtained from a turbofan engine after a long period of airline operation, these values being established in the range $R_a = 1.53-2.03$ μm. The roughness to be imposed on the test-rig blades, calculated by Gbadebo et al. [6], is about 25 μm, which corresponds to an equivalent sand grain roughness $k_s = 160$ μm. Regarding numerical simulations, Gbadebo et al. [6] used a 3D Navier–Stokes code, which uses a control volume formulation on a structured mesh, an eddy viscosity mixing length for turbulence modeling, and an ad hoc developed simple model to simulate roughness effects. The most interesting results can be summarized as follows: (i) Surface roughness typical of real engine operations can lead to a significant reduction in performance due to the effect on 3D separation; (ii) when tested as a stage, the 3D separation induced by roughness causes a significant loss in stage total pressure over a wide range of flow; (iii) the measured overall mass-averaged total pressure rise coefficient reduced by about 5.4% due to roughness, while the numerical simulations significantly underestimated this reduction (the calculated reduction in the mass-averaged total pressure rise coefficient was about 2.4%).

Other considerable contributions to this topic, which have recently appeared in literature, are the papers by Syverud et al. [7] and Syverud and Bakken [8]. In Ref. [7], test results from a series of accelerated deterioration tests on a GE J85-13 jet engine are presented. The axial compressor (eight stages, pressure ratio equal to 6.5) was deteriorated by spraying atomized droplets of saltwater into the engine intake. They noticed that the roughness of the rotor blade deposits are 50% of the roughness found on the stator vanes. They also found that surface roughness was not uniform and that the greatest roughness values were found on the pressure side of the vanes. Measured equivalent sand grain roughness values k_s were in the range $15-25$ μm for the pressure side and $2-15$ μm for the suction side, which correspond to relative surface roughness values k_s/c ranging from 0.6×10^{-4} to 11×10^{-4}. Regarding compressor performances, they found the following: (i) a shift of the compressor operating line to a lower flow rate and a lower pressure ratio and (ii) deterioration reduced both the stage work coefficient and the flow coefficient. In Ref. [8], the experimental results gathered in Ref. [7] were compared against models based on correlations in terms of loss estimates due to fouling. According to the authors, none of the frictional loss models proved to be effective in predicting the large variation in the measured total pressure coefficient from clean to deteriorated conditions. All the models considered capture the shift in flow coefficient but the degradation effect due to roughness in the stage performance was underpredicted.

3 Model Development

In order to investigate the effects of fouling on a compressor stage, the NASA Stage 37 test case was used as the baseline geometry. The geometry and performance data were gathered from Ref. [9]. Differently from other papers, in this paper the effort was focused on simulating the entire compressor stage (rotor and stator) rather than the rotor alone. This could lead to a lower accuracy of the computational model with respect to modeling the rotor alone, because of the presence of a rotor/stator interface model and of the assumptions inherent in the periodicity of the computational domain. However, the simulation of the entire compressor stage could give more thorough information on compressor stage performance deterioration. Hence, since the aim of this paper was to give an insight in the change in compressor stage performance caused by deterioration, the model development and validation focused on reproducing, as accurately as possible, the behavior of an axial compressor stage. This means that, rather than perfectly matching the experimental data of the original compressor, the numerical model has to correctly capture and reproduce the overall characteristics of an axial compressor, i.e., shape of the performance maps and main fluid dynamic features. Hence, the choices and the considerations in the following paragraphs should be read in this way. A similar methodology was used in Ref. [10], where the NASA Rotor 37 was used as the baseline geometry to investigate the influence of the sweep and the lean on the performance of transonic compressors.

3.1 Reference Compressor Stage. The NASA Stage 37 is composed of a rotor and a stator. Multiple circular arc blade profiles were used in the original design for all blade rows. The overall NASA Stage 37 performance at design point (corrected mass flow of 20.19 kg/s and rotational speed of 17,188 rpm) is a pressure ratio equal to 2.050 and an adiabatic efficiency equal to 0.842. The *rotor* is composed of 36 blades and is characterized by an inlet hub-to-tip diameter ratio of 0.7, a blade aspect ratio of 1.19 and a tip solidity of 1.29. The tip clearance at design speed is 0.356 mm (0.45% of the blade span). The rotor design pressure ratio and adiabatic efficiency are 2.106 and 0.877 and the design tip speed is 454 m/s, respectively. The *stator* is composed of 46 blades. Its blade aspect ratio is equal to 1.26 and its tip solidity is equal to 1.3.

3.2 Geometric Assumptions. To reduce computational effort, only a section of the full geometry has been modeled. Due to the impossibility of an ideal periodicity that could match both rotor and stator and in order to keep good accuracy while saving computational resources, the computational domain consisted of four rotor blades and five stator blades. This resulted in a 40.00° section for the rotor and a 39.13° section for the stator. This also resulted in a rotor/stator pitch ratio at the interface equal to 1.250 instead of 1.278 of the real geometry (2.2% difference). This approximation is handled by the code by scaling the flow that crosses the interface. In Fig. 1, a sketch of the computational domain is reported. The clearance at the rotor tip was also modeled and the relative motion between rotor and casing was included in the calculations. Tip clearance was set equal to 0.356 mm (equal to the tip clearance at design speed).

3.3 Numerical Code. The numerical simulations were carried out with the commercial CFD code ANSYS CFX 11.0 [11]. The code solves the 3D Reynolds-averaged form of the Navier–Stokes equations by using a finite-element based finite-volume method. An algebraic multigrid method based on the additive correction multigrid strategy was used. A second-order high-resolution advection scheme was adopted to calculate the advection terms in the discrete finite-volume equations.

3.4 Numerical Grid. The grids used in the calculations were hybrid grids generated by means of ANSYS ICEM CFD 11.0 [12]. The grids were realized by starting from a tetrahedral mesh and then by adding prism layers on the surface of the blades to help solve the boundary layer around the blade. The final mesh was composed of about 1,055,000 elements and nine prism layers (Fig. 1)

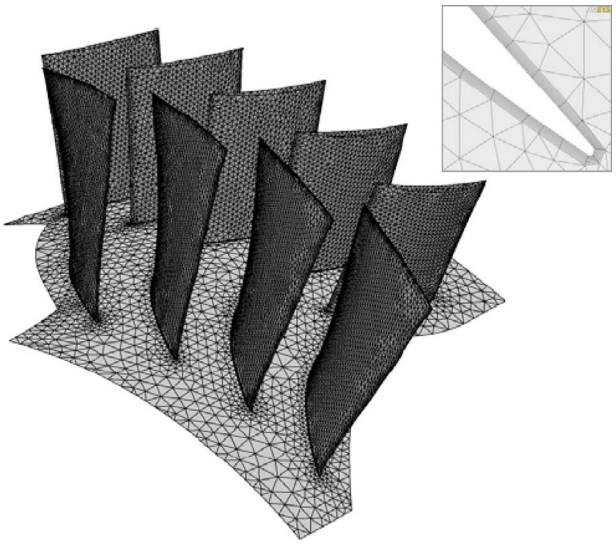

Fig. 1 Modeled geometry, numerical grid, and detail of the prism layer near blade surface for NASA Stage 37

and the first grid point height was fixed at 50 μm. These choices will be discussed later in this paper in Sec. 3.6.

3.5 Turbulence Model. Two turbulence models were used in the calculations: the Shear Stress Transport (SST) k-ω model and the standard k-ε model. In particular, the SST k-ω model was only used in the validation process, while the k-ε model was used both in the validation process and for the simulations when roughness was taken into account.

Near-wall effects are modeled by means of scalable wall functions in the k-ε model and by means of the automatic near-wall treatment method in the SST k-ω model. The near-wall treatment method automatically switches from a wall-function model to a low-Reynolds-number model as the mesh is refined.

In the code used for the calculations, the wall-function model used by the k-ε model uses empirical formulas that impose suitable conditions near the wall without resolving the boundary layer. In particular, the wall functions used are scalable wall functions. The scalable wall-function model can be applied on arbitrarily fine meshes and it allows a consistent mesh refinement independent of the Reynolds number [11]. Scalable wall functions are based on the analytical-wall-function approach (well documented in Ref. [13]), in which a modified turbulent velocity scale $\tilde{u}_\tau$ dependent on the turbulent kinetic energy at the near-wall node k_p is used:

$$\tilde{u}_\tau = C_\mu^{1/4} k_p^{1/2} \tag{1}$$

and, as a consequence, a modified y^+ based on $\tilde{u}_\tau$ can be obtained:

$$\tilde{y}^+ = \tilde{u}_\tau y/\nu \tag{2}$$

The basic idea behind the scalable wall-function approach is to limit the computed $\tilde{y}^+$ value used in the logarithmic formulation from falling below 11.06, which is the value assumed for the intersection between the logarithmic and the linear near-wall profile [11].

In any case, when theoretical fluid dynamic considerations are of concern, the y^+, u^+, and u_τ parameters have to be used in their usual form, i.e.,

$$u^+ = \frac{u_t}{u_\tau} = \frac{1}{\kappa}\ln(y^+) + C \tag{3}$$

$$y^+ = (\rho y u_\tau)/\mu \tag{4}$$

$$u_\tau = \sqrt{\tau_w/\rho} \tag{5}$$

3.6 Roughness Model. In order to account for surface roughness of deteriorated blades, the near-wall model of the k-ε turbulence model has to be modified. The near-wall functions as described above are appropriate when walls can be considered as hydraulically smooth. For rough walls, the logarithmic profile still exists but moves closer to the wall. As an index of the wall roughness, the equivalent sand grain k_s has been widely used by many researchers. This model was originally proposed by Schlichting [14]. It is an empirical model based on the similarity between (i) elements characterized by various shapes of roughness and (ii) data regarding the flow in pipes with a varying size of sieved sand glued to the surface taken from Nikuradse [15]. The equivalent sand grain index for a specific surface is assigned by comparing the velocity profile with profiles from Nikuradse surface. Schlichting [14] showed that the equivalent sand grain index was not only affected by the actual height of roughness but also by roughness shape and density, and so various correlations were proposed in literature [16].

Roughness effects can be accounted for by modifying the logarithmic profile as follows:

$$u^+ = \frac{u_t}{u_\tau} = \frac{1}{\kappa}\ln\left(\frac{\tilde{y}^+}{1 + 0.3 \cdot \tilde{k}^+}\right) + C \tag{6}$$

where

$$\tilde{k}^+ = \frac{k_s \tilde{u}_\tau}{\nu} \tag{7}$$

Equations (6) and (7) are coherent with the scalable wall functions definition. Equation (7) differs from the usual definition of k^+, Eq. (8) [17], which is instead coherent with the standard wall function formulation.

$$k^+ = \frac{k_s u_\tau}{\nu} \tag{8}$$

Once again, when theoretical fluid dynamic considerations are of concern, the parameter k^+ as in Eq. (8) has to be used. Three different regimes can be then defined as a function of k^+: (i) *hydraulically smooth regime* ($0 \le k^+ \le 5$), the friction factor depends only on Reynolds number since the size of roughness is so small that all the protrusions are contained within the laminar sublayer; (ii) *transition regime* ($5 \le k^+ \le 70$), the friction factor depends on Reynolds number and on the ratio k_s/R since the protrusions extend partly outside the laminar sublayer and the additional resistance is mainly due to the form drag experienced by the protrusions in the boundary layer; (iii) *completely rough regime* ($k^+ > 70$), the friction factor only depends on the ratio k_s/R since all the protrusions reach outside the laminar sublayer and by far the largest part of resistance to flow is due to the form drag that acts on them.

Regarding numerical calculations in the presence of roughness, a commonly accepted criterion states that wall-function approach can lead to low accuracy if the imposed k_s is of the same order or larger than the distance from the wall to the first grid point. Therefore, when roughness models are activated, the mesh should be checked properly against the imposed k_s values. Cadorin et al. [18] performed a validation and a sensitivity analysis on hybrid grids (tetrahedral core and prism layers near walls) against roughness models by varying the first grid point height, and the number and depth in the transverse direction of the prism layers. They showed that the models are highly capable of resolving the boundary layer in the presence of surface roughness. They also confirmed that the distance of the first grid point from the wall should be of the same order or larger than the equivalent sand grain roughness k_s imposed on the surface to be simulated. Nevertheless, they also found that the model can provide reasonable results by varying k_s independently of the first grid point height. For

these reasons, in this paper, a single grid, composed of about 1,055,000 tetrahedral elements, nine prism layers, and first grid point height fixed at 50 μm, was used.

3.7 Roughness in Compressor Blades. In turbomachinery calculations, the described method based on k^+ to distinguish between the hydraulically smooth regime and rough regimes can be difficult to apply. Therefore, Koch and Smith [19] proposed a method (originally theorized by Schlicting [17]) based on the definition of a roughness Reynolds number Re_k:

$$\mathrm{Re}_k = \frac{k_s W_1}{\nu} \tag{9}$$

where W_1 is the relative inlet velocity and ν is the cinematic viscosity of the fluid. The method states that a surface is hydraulically smooth if Re_k is lower than 90. This method (which is conceptually similar to the method based on k^+) allows a straightforward estimation of the hydraulic region.

3.8 Rotor/Stator Interaction Model. The simulations were performed in a steady multiple frame of reference to take into account the contemporary presence of moving and stationary domains. In particular, a mixing plane approach was imposed at the rotor/stator interface (which was located halfway between the two components) and used for all the simulations. In this approach, a single-pass steady-state solution is calculated exchanging the flow field variables at the interface. Flow field data are averaged circumferentially for both frames at the interface and passed to the adjacent zone as boundary conditions. This spatial averaging at the interface removes any unsteadiness generated in the zone-to-zone flow field, but the resulting solutions are often reasonable approximations of the time-averaged flow field.

3.9 Boundary Conditions. The total pressure, total temperature, and flow angle were imposed at the inflow boundary. The inlet total pressure and total temperature were fixed at $p_{01}=101{,}325$ Pa and $T_{01}=288.15$ K, respectively.

Regarding outflow boundary conditions, two different strategies were followed depending on the zone of the (m,β) performance map where the working point to be simulated is located. In fact, the slope of the curve is different when near-stall or near-choked flow regions are attained. Different conditions that have to be set to have uniqueness of the numerical solution are as follows.

- In the near-choked flow region, the (m,β) curve is almost at a constant flow rate. In this region, an average relative static pressure p_{r2} was imposed at the outflow boundary. The outflow pressure was progressively increased from $p_{r2}=0$ Pa until near-stall region is attained.
- In the near-stall region, the (m,β) curve is almost at constant pressure ratio. In this region, a mass flow rate was imposed at the outflow boundary. The mass flow rate was progressively decreased to simulate different working points. The absolute value of the mass flow rate depends on (i) the constant rotational speed map (100% design speed or 90% design speed) and (ii) the imposed roughness on the blade surface, which considerably alters the maximum mass flow achievable by the compressor stage.

Finally, since only a section of the full geometry has been modeled, rotational periodic boundary conditions were applied to the lateral surfaces of the flow domain.

4 Model Validation

As a first step, the model was validated against the experimental data reported in Ref. [9], which referred to a real but nondeteriorated compressor. The model was validated by using two turbulence models: the SST k-ω model and the standard k-ε model.

The validation particularly focuses on the k-ε model with the roughness model activated, since this is the model used when blade deterioration is considered in the calculation. For this reason, boundary conditions at walls were treated in a different way for the two turbulence models used.

For the SST k-ω, the walls were treated as smooth, while for the k-ε model, an equivalent sand roughness $k_s=1$ μm was set, which correspond to a roughness Reynolds number Re_k of about 25. This was done to (i) perform a first check on the applicability of the roughness model and (ii) check whether the surface behaves as smooth (Reynolds number Re_k lower than 90).

Particular attention has been devoted to the imposed angular velocity. Two different working conditions were considered, which in Ref. [9] are indicated as 100% and 90% of the design speed. However, the experimental data reported in Ref. [9] and used in this paper for the validation refer to five different readings in which the rotational speed varies in the range $n_{\mathrm{exp}}=17{,}169-17{,}254$ rpm for 100% design speed and $n_{\mathrm{exp}}=15{,}468-15{,}489$ rpm for 90% design speed. In the present context, however, it was preferred to fix a single rotational speed and to consider the variability of the experimental values as an additional uncertainty. Therefore, the imposed rotational speed for the two calculations was $n_{\mathrm{num}}=17{,}197$ rpm at 100% and $n_{\mathrm{num}}=15{,}470$ rpm at 90%.

4.1 Results and Discussion. In Fig. 2, the calculated and experimental performance maps are reported. The mass flow has been rendered non-dimensional by normalizing the data through the mass flow rate in choked condition (at 100% design speed). The value used for normalization was the calculated and the measured ones for numerical results and experimental data, respectively. The error bars reported for the experimental data do not refer to the actual experimental uncertainty, but are intended to fix a reference offset to judge the simulation validity. However, the error bar magnitude is related to a commonly achievable measurement uncertainty. The error bars are equal to $\pm 3\%$ of the reading for p_{03}/p_{01}, T_{03}/T_{01} and η_{is}. It can be noticed that:

- The shape of all the experimental performance maps is correctly reproduced by the numerical code, and the error between the calculated and measured values of the mass flow in choked condition at 100% rotational speed (used for the normalization) is about 1.4%. Since, as previously mentioned, the aim of the validation was to obtain a realistic compressor model rather than reproducing the NASA Stage 37 experimental data, the numerical model can be considered reliable. The nominal conditions of the numerical model, which will be used as a reference point in the following, are reported in Table 1. As can be noticed, the nominal conditions of the numerical model are quite close to the nominal condition of the real compressor stage (at 100% design speed, within 2% for each parameter).
- Anyway, the numerical values are in a fairly good agreement with the experimental data. The numerical results always underestimate the experimental data, but in a very consistent way. However, if the variability of the rotational speed is considered, due to both measurement uncertainty (± 30 rpm) and experimental repeatability, the agreement can be considered even more satisfactory.

The SST k-ω model seems to perform slightly better than the k-ε model. Nevertheless, the difference between the two models is almost negligible, and, as a consequence, the k-ε model with rough walls equal to $k_s=1$ μm can be considered hydraulically smooth.

The development of a reliable model also requires a correct reproduction of the main physical phenomena within the flow field [20]. In Fig. 3, shock structures at 0.7 rotor span for three characteristic working points (near stall, peak efficiency, and choked flow) are reported. The predicted shock structures are a good representation of the typical patterns for the characteristic working points. Other trends in flow characteristics (tip-clearance

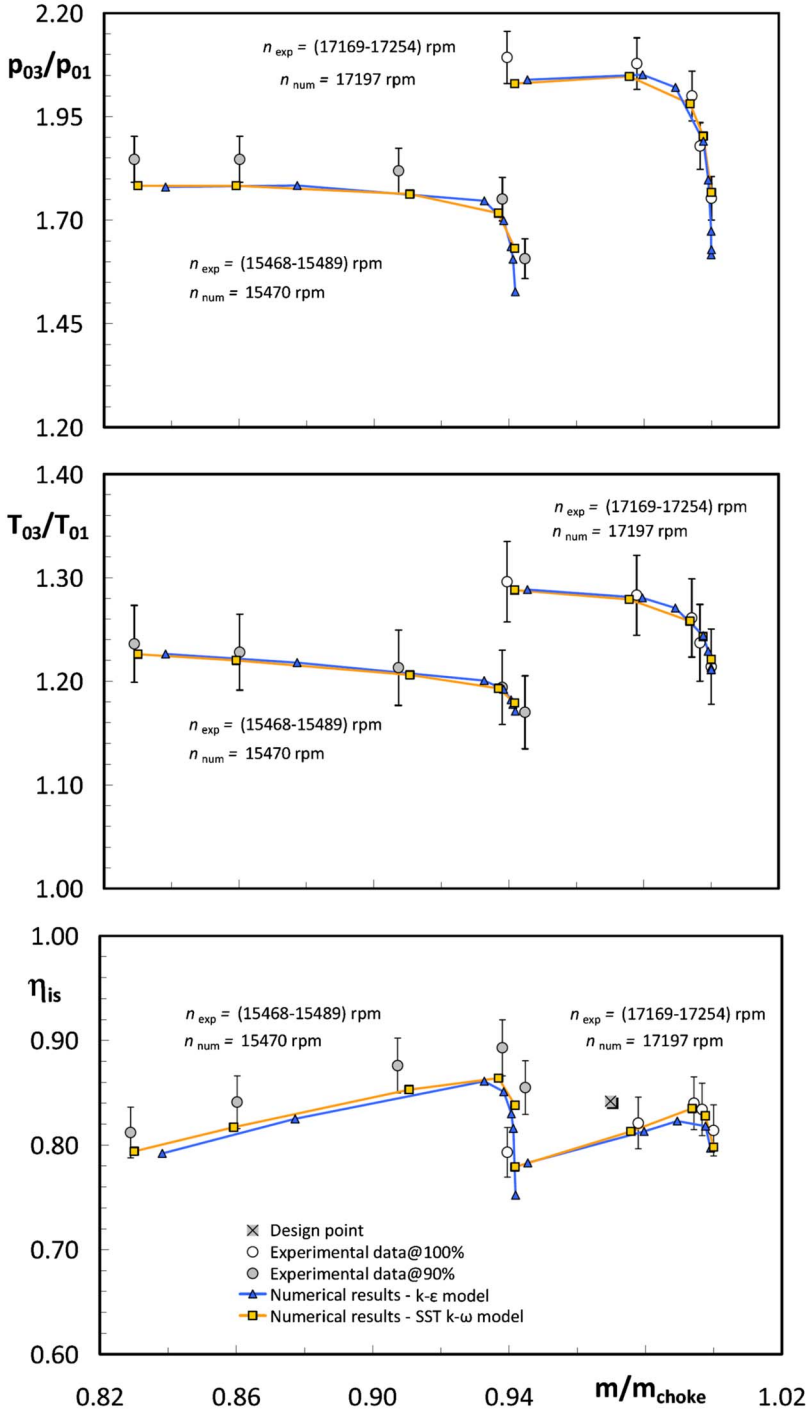

Fig. 2 Performance maps: comparison between experimental data and numerical results

Table 1 Maximum efficiency operating point values of numerical model and experimental compressor

	100% design speed		90% design speed	
	CFD model	Real stage	CFD model	Real stage
Mass flow (kg/s)	20.30	20.70	19.30	19.53
Pressure ratio	2.021	2.000	1.717	1.751
Adiabatic efficiency	0.823	0.835	0.864	0.893
Rotational speed (rpm)	17,197	-	15,470	

flows, blade wakes, etc.) were also well predicted by the model. Qualitative comparison performed with the data reported in Ref. [20], in which the experimental results referred to Rotor 37 alone rather than the entire stage, confirmed this statement.

5 Model Application to Blade Fouling

In this section, the compressor stage numerical model, which has previously set up and validated, is used to simulate the behavior of compressor stages when blade fouling occurs. Following the methodology carried out in Ref. [5], fouling on compressor stages was simulated by adding roughness and thickness to the blade

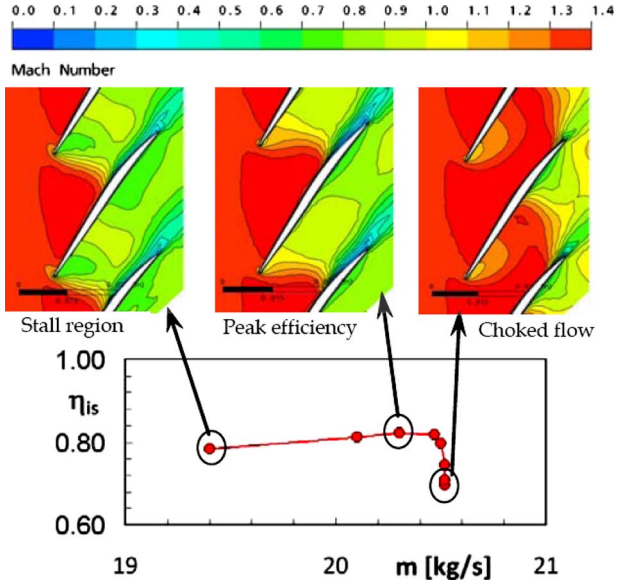

Fig. 3 Fluid dynamic features: shock structures at 100% design speed and at rotor span equal to 0.7

surface. Different from Refs. [5,6], in this paper, roughness and thickness were added to stator and rotor in order to predict the modifications in the performance of the entire stage rather than the rotor alone. Moreover, modifications were imposed on all the relevant blade surfaces (suction side, pressure side, leading edge, and trailing edge), and on their entire extension from inlet to outlet and from hub to shroud (100% pressure side and suction side surface coverage). The modifications on the airfoil surfaces were carried out as follows.

- The surface roughness was taken into account by means of the roughness model outlined above. In particular, three different k_s values were imposed. The correspondent R_a is related empirically to k_s: Its value can be found by using the dividing coefficient of 6.2 proposed in Ref. [19]. In Table 2, these values are reported together with the relative roughness values k_s/c. These latter values are of the same order of magnitude as the values usually found in literature [4–7]. Two surface roughness values, $R_a=\{0.81,6.45\}$ μm, are typical values for the actual axial compressor surface finish in the presence of different levels of fouling [5–7]. In contrast, the value $R_a=12.1$ μm was chosen in order to magnify the effect of the surface roughness, since it has been proved that the numerical models usually underestimate the actual influence of surface roughness on the compressor overall performance [5,6].
- The magnitude of the added thickness Δt_b was chosen in order to (i) simulate the presence of dust and particles, which could have stuck on the airfoil surface and, thus, alter the geometry of the airfoil, and (ii) take into account that roughness models can usually significantly underestimate the real effect of surface roughness, as stated above [5,6]. For this reason, the added thickness was magnified with respect to the actual values reported in literature, in order to partially compensate underestimation issues of the roughness models. Hence, the added thickness Δt_b was set equal to 0.3 mm.

Table 2 Parameters for fouling simulation

	Δt_b (mm)	k_s (μm)	R_a (μm)	k_s/c	Re_k	Regime
Base-S	-	1	0.16	1.77×10^{-5}	25	Smooth
Base-R	-	40	6.45	7.14×10^{-4}	993	Rough
Thick-S	+0.3	1	0.16	1.77×10^{-5}	25	Smooth
Thick-R1	+0.3	5	0.81	8.93×10^{-5}	124	Rough
Thick-R2	+0.3	40	6.45	7.14×10^{-4}	993	Rough
Thick-R3	+0.3	75	12.1	1.34×10^{-3}	1869	Rough

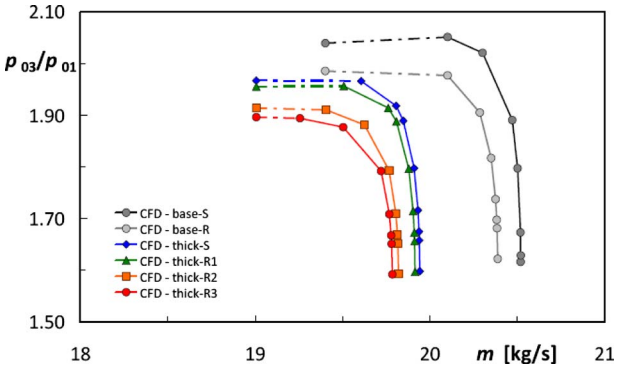

Fig. 4 Compressor stage performance curve: pressure ratio versus mass flow

Following these assumptions, different fouling conditions were simulated. The baseline simulation was chosen to be the initial geometry with no thickness and surface alteration, thus representing the compressor in new and clean condition (base-S). Then, the airfoil thickness was kept constant and a roughness value equal to $k_s=40$ μm ($R_a=6.45$ μm) was imposed on the blade surface (base-R). This latter simulation was intended to set a reference level of the influence of roughness on compressor performances. Subsequently, four different increasing-in-severity fouling conditions were simulated by imposing different combinations of the constant thickness increase $\Delta t_b=+0.3$ mm and different surface roughness levels $R_a=\{0.16,0.81,6.45,12.1\}$ μm. A summary of these assumptions is reported in Table 2.

5.1 Compressor Characteristic Maps. Simulated compressor performance curves at 100% design speed are reported in Fig. 4. As can be seen, the main effect of fouling is the decrease in mass flow rate. This decrease is higher when fouling condition becomes more severe (from 0.7% decrease for base-R to 3.6% decrease for thick-R3). However, if a plausible compressor working line is followed, it is possible to also notice a decrease in the stage compressor ratio.

In compressor applications that require a constant pressure rise, such as pipeline pumping and stationary power generation, loss levels can be assessed by plotting efficiency against pressure ratio [5]. As can be noticed in Fig. 5, when there is a rough surface without thickness increase, the efficiency loss at a constant pressure ratio is almost negligible in the choked flow region ($\beta=1.60-1.75$) and gradually increases up to nearly 2% close to the near-stall region ($\beta\geq1.95$). When the thickness increases, in the choked flow region the same efficiency loss with respect to the base case can be observed for all the surface roughness values considered, as well as for the smooth surface. Moreover, the loss is approximately 2% regardless of surface roughness in the completely choked flow region, $\beta=1.60-1.65$, and ranges from 2% to 4% for $\beta=1.65-1.75$. From the above considerations, it can be seen that efficiency loss in the choked flow region could be entirely due to blockage while surface roughness has a negligible effect (where it does not contribute to the increase in blockage effects). Moreover, the maximum efficiency reduction at constant pressure ratio is about 6%, which is in the order of magnitude of similar results reported in Ref. [5].

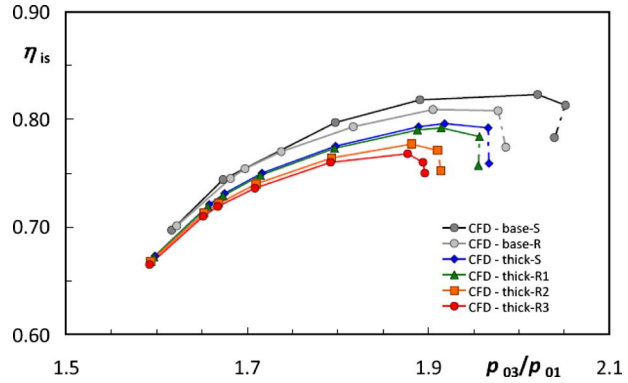

Fig. 5 Compressor stage performance curve: efficiency versus pressure ratio

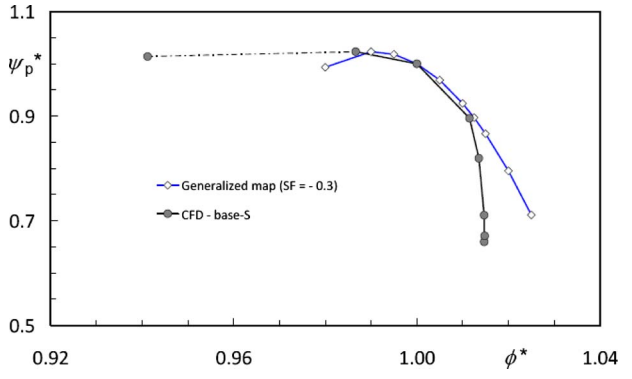

Fig. 6 Comparison between CFD results and values predicted through Eq. (10)

5.2 Compressor Stage Performance Coefficients. Thermodynamic-based models are widely used for the simulation of gas turbine operation both in steady-state and transient conditions. For these models, the knowledge of compressor performance maps is required. In the absence of the specific machine performance maps, which are proprietary of the manufactures, either generalized nondimensional overall compressor maps or stage-stacking models can be used within the thermodynamic models.

In particular, stage-stacking models use stage generalized relationships in order to obtain overall multistage compressor performance maps (which link together overall pressure ratio, efficiency, corrected mass flow, and corrected rotational speed) by means of a stage-by-stage procedure. This procedure has been developed and applied by the authors in previous papers [1,2].

In Ref. [1], a single generalized curve in terms of the generalized relationship, $\psi_p^* = \psi_p^*(\phi^*, SF)$, was set up based on the work of Muir et al. [21] by fitting experimental data points over a large number of compressor stages. To account for different stage characteristics based on different stage types, a parameter called shape factor SF was introduced to obtain a number of generalized curves covering all experimental data points reported in Ref. [21]. Therefore, the equation of the generalized curves, which is also used in this paper, is as follows:

$$\psi_p^* = \psi_{p,\max}^* - \frac{(\psi_{p,\max}^* - 1)\cdot[\phi_{\psi_{p,\max}}^* + SF\cdot(\phi_{\psi_{p,\max}}^* - 1) - \phi^*]^2}{[\phi_{\psi_{p,\max}}^* + SF\cdot(\phi_{\psi_{p,\max}}^* - 1) - 1]^2} \tag{10}$$

In Ref. [1], a relationship, $\eta^* = \eta^*(\psi_p^*/\phi^*)$, was obtained from the generalized stage efficiency curve proposed by Howell and Bonham [22]:

$$\eta^* = 1 - \frac{1 - \eta^*_{(\psi_p/\phi)_{\min}}}{\left[1 - \left(\frac{\psi_p^*}{\phi^*}\right)_{\min}\right]^{3.5}}\left(1 - \frac{\psi_p^*}{\phi^*}\right)^{3.5}, \quad \frac{\psi_p^*}{\phi^*} \in \left[\left(\frac{\psi_p^*}{\phi^*}\right)_{\min}, 1\right] \tag{11a}$$

$$\eta^* = 1 - \frac{1 - \eta^*_{(\psi_p/\phi)_{\max}}}{\left[\left(\frac{\psi_p^*}{\phi^*}\right)_{\max} - 1\right]^2}\left(\frac{\psi_p^*}{\phi^*} - 1\right)^2, \quad \frac{\psi_p^*}{\phi^*} \in \left[1, \left(\frac{\psi_p^*}{\phi^*}\right)_{\max}\right] \tag{11b}$$

This curve, together with the curves $\psi_p^*(\phi^*, SF)$, allows $\eta^*(\phi^*, SF)$ curves for all types of compressor stages to be obtained.

The predictions of the numerical model developed in this paper were compared against the generalized relationship $\psi_p^* = \psi_p^*(\phi^*, SF)$ and $\eta^* = \eta^*(\psi_p^*/\phi^*)$. To do this, the numerical results were processed in order to obtain the performance maps in terms of the nondimensional flow coefficient ϕ^*, pressure coefficient ψ_p^*, and isentropic efficiency η^*.

In Fig. 6, the comparison between numerical results for the healthy stage (base-S model) and the values obtained from the generalized relationship as in Eq. (10) is reported. The $\psi_p^* = \psi_p^*(\phi^*, SF)$ curve is calculated by assuming $SF = -0.3$. It can be observed that (i) even if Eq. (10) is a heuristic representation of experimental data, numerical results are in excellent agreement with the generalized curve from the near-stall region to the choked flow region ($0.98 < \phi^* < 1.01$); (ii) in the choked region ($\phi^* > 1.01$), the two curves rapidly diverge. This is probably due to the fact that the generalized curves derived from Ref. [21] are more representative of subsonic stages. NASA Stage 37 is instead a transonic stage, characterized by a tip Mach number $M_u = 1.38$, whose (ψ_p^*, ϕ^*) curves present an abrupt drop of ψ_p^* due to choked flow.

In Fig. 7, the comparison between numerical results for the healthy stage (base-S model) and the values obtained from the generalized relationship as in Eqs. (11*a*) and (11*b*) are reported. As can be seen, the agreement can be considered satisfactory only when it is close to the design point (ψ_p^*/ϕ^* in the range [0.8, 1.0]). Similarly, this seems mainly due to the fact that the Howell and Bonham curve was fitted to experimental measurements and calculated data regarding subsonic stages, which are characterized by a maximum efficiency point lying between the design point and the surge point. NASA Stage 37 is instead a transonic stage and its maximum efficiency point lies between the design point and the choked flow region (see Fig. 2). However, Eqs. (11*a*) and (11*b*) are still heuristic representations of experimental data but with a

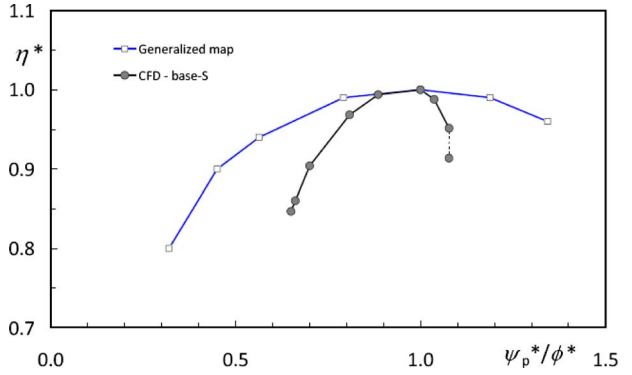

Fig. 7 Comparison between CFD results and values predicted through Eqs. (11*a*) and (11*b*)

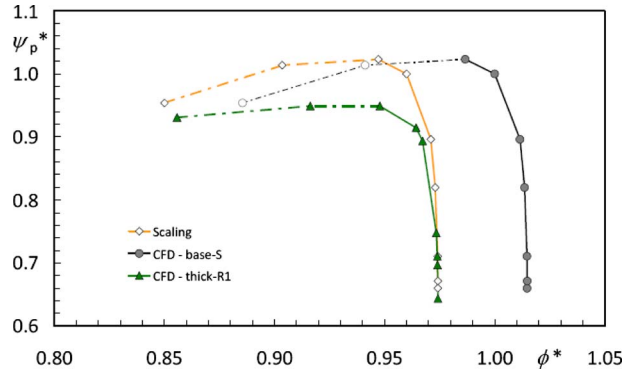

Fig. 8 (ϕ, ψ_p) curves for healthy CFD stage, fouled CFD stage, and fouled scaled stage

lower degree of confidence. This comparison suggests that the Howell and Bonham [22] curve should be updated by means of more recent experimental investigations and by means of fully validated computational models.

In Refs. [1,2], fouling was modeled through a decrease in the flow passage area, coupled with a decrease in efficiency, as usually performed in literature [23–29]. This stage performance scaling procedure leads to a decrease in the flow coefficient ϕ at a given pressure coefficient ψ_p.

The numerical model developed was used as a reference model to compare the numerical fouled curves with the fouled curves obtained by means of the scaling procedure. In Fig. 8, three curves (ϕ^*, ψ_p^*) are reported, which refer to base-S simulation, which represents the healthy stage performance, thick-R1 simulation, which represents the fouled stage performance obtained by means of the numerical simulation, and scaling model, which is calculated by means of a scaling procedure applied to base-S data. The scaling procedure was presented in Ref. [2]. It is performed by multiplying by a constant scale factor the calculated flow coefficient ϕ at a given calculated pressure coefficient ψ_p.

It can be observed that the assumptions inherent in the scaling procedure are not fully corroborated by numerical simulations. In fact, map scaling can correctly represent the behavior of the fouled stage in the choked flow region, but it does not capture the decrease in the maximum of the pressure coefficient ψ_p, which is instead highlighted by the numerical simulations.

This suggests that when the scaling procedure is used to simulate the change in compressor characteristic maps, a scale should also be applied to the pressure coefficient. Regarding numerical results, it can be observed that the fouling simulated in this paper, by adding thickness and roughness, induces a reduction in the flow coefficient in choked flow conditions by about 5% and a reduction in the pressure coefficient by nearly 9%. These values are of the same order of magnitude of experimental results found in literature [4–8]. Therefore, the model developed seems to overcome some of the limitations of the other CFD models found in literature, which tends to significantly underestimate the actual values of performance reduction.

5.3 Blockage Evaluation. Blockage is one of the fluid dynamic phenomena that influences the performance of compressor stages the most [30]. Blockage can be interpreted as a core flow effective reduction due to the presence of the boundary layer. As an index of the blockage, the boundary layer displacement thickness δ^* defined as

$$\delta^* = \int_0^{L/2} \left(1 - \frac{u}{u_E}\right) dy \tag{12}$$

is often used. Equation (12) is valid for flow in an axisymmetrical duct in which L is a characteristic dimension, y is the coordinate normal to the duct surface, u is the axial velocity, and u_E is the inviscid region axial velocity. In the present paper, a different approach was followed in order to account for tridimensional flow field effects on blockage. Following Refs. [31,32], a blockage parameter B is used:

$$B = 1 - \frac{A_{\text{flow}}}{A_{\text{geo}}} \tag{13}$$

where A_{geo} is the geometric area of the blade-to-blade plane on which blockage is calculated. The effective flow area A_{flow} is then calculated as follows:

$$A_{\text{flow}} = \int_{A_{\text{geo}}} \frac{\rho \mathbf{u} \cdot \mathbf{n}}{\rho_E \mathbf{u}_E \cdot \mathbf{n}} dA \tag{14}$$

where n is the outer normal of the blade-to-blade plane on which blockage is calculated. Since it is not straightforward to determine the inviscid velocity and density [30–32], Eq. (14) is redefined as follows:

$$A_{\text{flow}} = \int_{A_{\text{geo}}} \frac{\rho \mathbf{u} \cdot \mathbf{n}}{\rho|_{\max(\mathbf{u}_E \cdot \mathbf{n})} \max(\mathbf{u}_E \cdot \mathbf{n})} dA \tag{15}$$

Table 3 Quantification of blockage

	B	ΔB (%)	ΔA_{flow} (%)
Base-S	0.108	-	-
Base-R	0.123	13.9	−1.7
Thick-S	0.138	27.8	−3.5
Thick-R1	0.145	34.3	−4.3
Thick-R2	0.166	53.7	−7.0
Thick-R3	0.174	61.1	−8.0

In Table 3, the values of blockage for the different fouling conditions (see Table 2) are reported, which are calculated on a blade-to-blade plane approximately normal to streamlines at rotor outlet. In order to highlight the effect of simulated fouling (roughness and added thickness) on the performance of the stage, the geometric area taken into consideration for all the configurations is the base-S geometric area, i.e., the area of the healthy stage. So, for the thickened geometry, the velocity is set at zero in the passing area that is occupied by the blade added thickness. All simulations refer to choked flow region.

It can be noticed that an increase in blade roughness modifies the flow field and leads to an increase in the blockage (13.9% for base-R with respect to base-S). Moreover, also a variation in thickness alone leads to a modification of the flow field. In fact, by analyzing the differences between the base-S simulation (original thickness and smooth surface) and the thick-S simulation (added thickness and smooth surface), it can be seen that, while the added thickness (Δt_b=+0.3 mm) corresponds to a geometric area decrease of only 1.6%, the variation in the effective flow area ΔA_{flow} is equal to −3.5%, which corresponds to a blockage increase of 27.8%. Moreover, the results reported in Table 3 corroborate the assumptions made in Ref. [1], where a variation up to 10% of the effective flow area was considered, to perform the stage-stacking calculations in the presence of fouling.

Interesting considerations can be drawn by analyzing Fig. 9, where lines of constant entropy are represented in order to highlight the effect of thickness and roughness on the boundary layer. In Fig. 9(*a*), the entropy constant line for base-S simulation in the peak efficiency condition is presented. An abrupt variation in the boundary layer is highlighted on the suction surface due to the impingement of the passage shock on the blade (see Fig. 3). This result is in agreement with the results reported in Ref. [5] and represents a further validation of the model. In Fig. 9(*b*), base-S, thick-S, and thick-R3 conditions are compared by using simula-

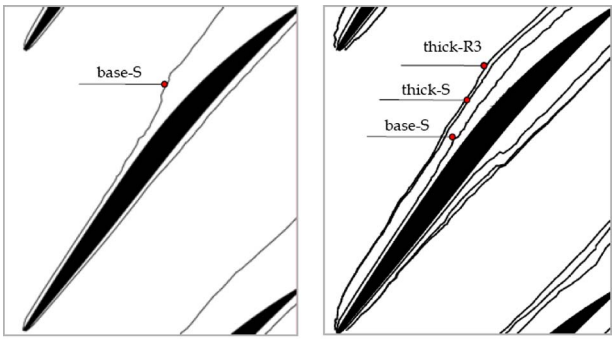

Fig. 9 Constant entropy lines for boundary thickness increase evaluation: (*a*) peak efficiency and (*b*) choked flow region

tion in choking conditions. It can be noticed that both thickness addiction and roughness increase lead to a thickening of the boundary layer both in the suction surface and in the pressure surface. Moreover, the boundary layer is thicker in the suction surface than in the pressure surface. The abrupt variation in the boundary layer is highlighted in the pressure surface, which differs from the previous results where, in contrast, the step-change variation is located on the suction surface. This is due to the fact that the impingement occurs at the pressure surface midchord in the case of choking, while it occurs at midchord in the suction surface in the case of peak efficiency (see Fig. 3).

6 Conclusions

In this paper, numerical simulations of fouling affecting an axial compressor stage were carried out. To do this, the NASA Stage 37 was considered for the numerical investigation, which was performed by means of a commercial CFD code. The code, set up against experimental data taken from literature, allowed a representative model of a realistic compressor stage to be obtained both in terms of overall performance and of fluid dynamic features.

Then, the model was used to simulate the occurrence of fouling by imposing different combinations of added thickness and surface roughness levels in order to estimate the performance modification of axial compressor stages due to fouling. The results highlighted that (i) the main effect of fouling is the decrease in the flow rate, which is higher when fouling condition becomes more severe, but a decrease in the stage compressor ratio was also noticed; (ii) efficiency loss in the choked flow region could be entirely due to blockage while surface roughness has little effect (where it does not contribute to increase blockage effects).

Moreover, the common stage performance scaling procedure used in stage-stacking models in order to represent fouling in multistage compressors was analyzed. The numerical results highlighted that the assumptions inherent in the scaling procedure should be revised. In fact, the scaling can correctly represent the behavior of the fouled stage in the choked flow region, but it does not capture the decrease in the maximum of the pressure coefficient, which is instead revealed by the numerical simulations.

It was also observed that the type of fouling simulated in this paper, by adding thickness and roughness, induces reductions in the flow and pressure coefficients that are of the same order of magnitude as the experimental results found in literature. Therefore, the model developed seems to overcome some of the limitations of other models found in literature, which tend to significantly underestimate the actual values of performance reduction.

Finally, an analysis of boundary layer growth and the consequent increase in blockage was carried out. This analysis confirmed that the developed model can correctly capture the physics of the phenomena that occur inside a fouled compressor stage both at a macro- and at a microscale level.

Acknowledgment

The authors gratefully acknowledge Professor Roberto Bettocchi for the support given throughout the project. The authors would like to thank Marco Mistrin, M.Sc., for his valuable work in developing the geometrical model, and Giulio Cenci, Ph.D., for the helpful suggestions.

Nomenclature

A = area
B = blockage parameter
C_μ = model constant, Eq. (1)
c = chord
C = constant
D = diameter
h = specific enthalpy
k = turbulent kinetic energy
k_s = equivalent sand grain
k^+ = nondimensional roughness height
$\tilde{k}^+$ = modified nondimensional roughness height
L = characteristic dimension
m = mass flow rate
M = Mach number
$\mathbf{n}$ = plane normal versor
p = pressure
$\mathbf{n}$ = pipe radius
R_a = center line average (CLA) roughness
Re_k = roughness Reynolds number
SF = shape factor
t = thickness
T = temperature
u = velocity
u_t = velocity tangent to the wall
u^+ = nondimensional velocity
u_τ = friction velocity
$\tilde{u}_\tau$ = modified friction velocity
U = blade speed at the mean radius
V = absolute flow velocity
W = relative velocity
x = axial distance, Cartesian coordinate
y = normal distance, Cartesian coordinate
y^+ = nondimensional distance
$\tilde{y}^+$ = modified nondimensional distance
β = pressure ratio
ε = dissipation rate of turbulent kinetic energy
δ^* = displacement thickness
Δ = variation
η = efficiency
ρ = density
κ = model constant, Eq. (6)
μ = dynamic viscosity
ν = kinematic viscosity
τ = shear stress
ω = turbulent frequency
ϕ = V_a/U flow coefficient
ψ_p = $\Delta h_{0\mathrm{is}}/U^2$ pressure coefficient

Subscripts and Superscripts

0 = total
1 = stage inlet
3 = stage outlet
a = axial
b = blade
choke = choked condition
is = isentropic
E = inviscid
exp = experimental
flow = effective flow

geo = geometric
num = numerical
P = near-wall node
r = relative
u = tip velocity
τ = shear
w = wall
$*$ = normalized value with respect to peak efficiency value

References

[1] Morini, M., Pinelli, M., Spina, P. R., and Venturini, M., 2010, "Influence of Blade Deterioration on Compressor and Turbine Performance," ASME J. Eng. Gas Turbines Power, **132**(3), p. 032401.
[2] Spina, P. R., 2002, "Gas Turbine Performance Prediction by Using Generalized Performance Curves of Compressor and Turbine Stages," ASME Paper No. GT-2002-30275.
[3] Kurz, R., Brun, K., and Wollie, M., 2009, "Degradation Effects on Industrial Gas Turbines," ASME J. Eng. Gas Turbines Power, **131**(6), p. 062401.
[4] Bammert, K., and Woelk, G. U., 1979, "The Influence of the Blading Surface Roughness on the Aerodynamic Behavior and Characteristic of an Axial Compressor," ASME Paper No. 79-GT-102.
[5] Suder, K. L., Chima, R. V., Strazisar, A. J., and Roberts, W. B., 1995, "The Effect of Adding Roughness and Thickness to a Transonic Axial Compressor Rotor," ASME J. Turbomach., **117**(4), pp. 491–505.
[6] Gbadebo, S. A., Hynes, T. P., and Cumpsty, N. A., 2004, "Influence of Surface Roughness on Three-Dimensional Separation in Axial Compressors," ASME J. Turbomach., **126**(4), pp. 455–463.
[7] Syverud, E., Brekke, O., and Bakken, L. E., 2007, "Axial Compressor Deterioration Caused by Saltwater Ingestion," ASME J. Turbomach., **129**, pp. 119–127.
[8] Syverud, E., and Bakken, L. E., 2006, "The Impact of Surface Roughness on Axial Compressor Performance Deterioration," ASME Paper No. GT-2006-90004.
[9] Reid, L., and Moore, R. D., 1978, "Design and Overall Performance of Four Highly-Loaded, High-Speed Inlet Stages for an Advanced High-Pressure-Ratio Core Compressor," NASA Report No. TP 1337.
[10] Benini, E., and Biollo, R., 2007, "Aerodynamics of Swept and Leaned Transonic Compressor-Rotors," Appl. Energy, **84**, pp. 1012–1027.
[11] ANSYS CFX 11.0, 2007, User Manual.
[12] ICEM CFD 11.0, 2007, User Manual.
[13] Apsley, D., 2007, "CFD Calculation of Turbulent Flow With Arbitrary Wall Roughness," Flow Turbul. Combust., **78**, pp. 153–175.
[14] Schlichting, H., 1936, "Experimental Investigation of the Problem of Surface Roughness," NACA Report No. TM 823.
[15] Nikuradse, J., 1933, "Laws of Flow in Rough Pipes," NACA Report No. TM 1292.
[16] Sigal, A., and Danberg, J. E., 1990, "New Correlation of Roughness Density Effect on the Turbulent Boundary Layer," AIAA J., **28**(3), pp. 554–556.
[17] Schlichting, H., 1960, *Boundary Layer Theory*, 4th ed., McGraw-Hill, New York.
[18] Cadorin, M., Morini, M., and Pinelli, M., 2009, "Numerical Analyses of High Reynolds Number Flow of High Pressure Fuel Gas Through Rough Pipes," ASME Paper No. GT-2009-59243.
[19] Koch, C. C., and Smith, L. H., 1976, "Loss Sources and Magnitudes in Axial Flow Compressors," ASME J. Eng. Gas Turbines Power, **98**, pp. 411–424.
[20] Benini, E., and Biollo, R., 2006, "Validation of a Navier–Stokes Solver for CFD Computations of Transonic Compressors," ASME Paper No. ESDA-2006-5318.
[21] Muir, D. E., Saravanamuttoo, H. I. H., and Marshall, D. J., 1989, "Health Monitoring of Variable Geometry Gas Turbines for the Canadian Navy," ASME J. Eng. Gas Turbines Power, **111**, pp. 244–250.
[22] Howell, A. R., and Bonham, R. P., 1950, "Overall and Stage Characteristics of Axial Flow Compressors," Proc. IMechE, **163**, pp. 235–248.
[23] Saravanamuttoo, H. I. H., and Lakshminarasimha, A. N., 1985, "A Preliminary Assessment of Compressor Fouling," ASME Paper No. 85-GT-153.
[24] Aker, G. F., and Saravanamuttoo H. I. H., 1988, "Predicting Gas Turbine Performance Degradation Due to Compressor Fouling Using Computer Simulation Techniques," ASME Paper No. 88-GT-206.
[25] Seddigh, F., and Saravanamuttoo, H. I. H., 1990, "A Proposed Method for Assessing the Susceptibility of Axial Compressors to Fouling," ASME Paper No. 90-GT-348.
[26] Tabakoff, W., Lakshminarasimha, A. N., and Pasin, M., 1990, "Simulation of Compressor Performance Deterioration Due to Erosion," ASME J. Turbomach., **112**, pp. 78–83.
[27] Massardo, A., 1991, "Simulation of Fouled Axial Multistage Compressors," IMechE Paper No. C423/048.
[28] Massardo, A., 1991, "An Analytical Method for the Fault Diagnosis of Axial Multistage Compressors," ASME Paper No. 91-GT-66.
[29] Lakshminarasimha, A. N., Boyce, M. P., and Meher-Homji, C. B., 1994, "Modeling and Analysis of Gas Turbine Performance Deterioration," ASME J. Eng. Gas Turbines Power, **116**, pp. 46–52.
[30] Greitzer, E. M., Tan, C. S., and Graf, M. B., 2004, *Internal Flows—Concepts and Applications*, Cambridge University Press, Cambridge.
[31] Cumpsty, N. A., 1989, *Compressor Aerodynamics*, Longmann, Harlow, UK.
[32] Suder, K. L., 1996, "Experimental Investigation of the Flow Field in a Transonic, Axial Flow Compressor With Respect to the Development of Blockage and Loss," NASA Report No. TM 107310.